

Detection of Pristine Gas Two Billion Years after the Big Bang

Michele Fumagalli^{1*}, John M. O’Meara², and J. Xavier Prochaska³

¹Department of Astronomy and Astrophysics, UC Santa Cruz, CA

²Department of Chemistry and Physics, Saint Michael’s College, Colchester, VT

³University of California Observatories-Lick Observatory, UC Santa Cruz, CA

*To whom correspondence should be addressed; E-mail: mfumagalli@ucolick.org

In the current cosmological model, only the three lightest elements were created in the first few minutes after the Big Bang; all other elements were produced later in stars. To date, however, heavy elements have been observed in all astrophysical environments. We report the detection of two gas clouds with no discernible elements heavier than hydrogen. These systems exhibit the lowest heavy-element abundance in the early universe and thus are potential fuel for the most metal poor halo stars. The detection of deuterium in one system at the level predicted by primordial nucleosynthesis provides a direct confirmation of the standard cosmological model. The composition of these clouds further implies that the transport of heavy elements from galaxies to their surroundings is highly inhomogeneous.

In modern cosmological theory, the light elements and their isotopes are produced during the first few minutes after the Big Bang when the universe cools during expansion from temperatures $T \sim 10^9$ K to below $\sim 4 \times 10^8$ K. In this brief epoch, termed Big Bang Nucleosynthesis (BBN), D, ^3He , ^4He , and ^7Li are synthesized with an abundance ratio relative to hydrogen that is sensitive to the cosmic density of ordinary matter (i.e. the baryon density $\Omega_{b,0}$). BBN theory also predicts negligible production of the heavy elements with abundance ratios $X/\text{H} < 10^{-10}$ and one must await the physical conditions that are typical of the stellar interiors (*I*).

The analysis of gas observed in absorption along the lines-of-sight to high-redshift quasars, distant galaxies that host supermassive black holes, is a powerful probe of the BBN yields. Particular attention has been given to deuterium, partly due to observational convenience but also because the D/H abundance ratio is very sensitive to $\Omega_{b,0}$. For quasar sight lines, the measured $\log(\text{D}/\text{H}) = -4.55 \pm 0.03$ (2, 3) translates into $\Omega_{b,0}h^2(\text{BBN}) = 0.0213 \pm 0.0010$, which is fully consistent with the value inferred from the Cosmic Microwave Background (CMB) power

spectrum $\Omega_{b,0}h^2(\text{CMB}) = 0.02249^{+0.00056}_{-0.00057}$ (WMAP7 (4)). This excellent agreement between two essentially independent experiments stands as a marked triumph of the Big Bang theory.

On the other hand, all of the systems with measured D have heavy-element abundances that exceed, by many orders of magnitude, the BBN prediction. In fact, despite measurement of thousands of galaxies from the early universe (e.g. (5, 6)) and careful study of the diffuse gas that permeates the universe (e.g. (7, 8)), one has yet to detect anything near primordial enrichment. For structures denser than the mean cosmic density (Fig. 1), the high-redshift universe has exhibited a floor in the metallicity Z , the mass fraction of elements heavier than hydrogen, at $\sim 1/1000$ of the solar abundance (Z_{\odot}). Similarly, among several old and iron-poor stars, only one has a metallicity $Z \sim 10^{-4}Z_{\odot}$ (9), with all the remaining having enhanced C or O abundances. The existence of a minimum level of enrichment at about $1/1000$ solar has been associated with the metal production in Population III (PopIII) stars, primordial stars that form in metal free environments via H_2 cooling. In fact, models and numerical simulations (e.g. (10, 11)) show that ejecta from this first stellar population can enrich the interstellar medium (ISM) of the host halos up to $\sim 10^{-3}Z_{\odot}$ and pollute the surrounding intergalactic medium (IGM) as soon as 1 billion years after the Big Bang ($z \sim 6$).

In this work, we report on the hydrogen and metal properties of two gas ‘clouds’ at $z \sim 3$, when the universe was only two billion years old. We observed quasars SDSS J113418.96+574204.6 ($z_{\text{em}} = 3.522$) and Q0956 + 122 ($z_{\text{em}} = 3.297$) on UT January 3 and 5, 2006 and UT April 7, 2006 with the HIRES spectrometer on the Keck I telescope on Mauna Kea (see SOM text 1). Previous low-resolution spectra of these quasars from the Sloan Digital Sky Survey had shown significant absorption at wavelengths $\lambda < 4000\text{\AA}$ characteristic of substantial optical depth τ_{LL} at the H I Lyman limit (at wavelength $\lambda < 912\text{\AA}$), typical of the Lyman limit systems (LLSs).

Our Keck/HIRES spectrum of J1134+5742 reveals a sharp break in the flux at $\sim 4000\text{\AA}$, indicating the presence of a LLS at $z \sim 3.4$ with $\tau_{\text{LL}} > 2$ (hereafter named LLS1134; Fig. 2), confirming the lower resolution data. A search for absorption lines at a redshift consistent with the Lyman break further reveals the presence of the H I Lyman series through to Lyman-22 (H I 913.5), corresponding to $\lambda \sim 4030\text{\AA}$. In the high resolution spectrum, two distinct absorbers can be identified within LLS1134, the main system (hereafter LLS1134a) at $z = 3.410883$ and a weaker component (named LLS1134b) at $z = 3.41167$, separated by $\delta v \sim 54\text{ km s}^{-1}$. In contrast, two flux decrements in the normalized HIRES spectrum of Q0956 + 122 (Fig. 3) are visible at $\sim 3860\text{\AA}$ and $\sim 3750\text{\AA}$, revealing the presence of two LLSs with $\tau_{\text{LL}} \sim 1$ at $z \sim 3.22$ (LLS0956A) and $z \sim 3.10$ (LLS0956B).

A closer inspection of these spectra also reveals no detectable metal-line absorption at the velocity of the strongest H I component for neither LLS1134a nor LLS0956B. Such a complete absence of heavy element absorption has not been previously reported for data with comparable sensitivity. For LLS1134a, besides the H I Lyman series, the only other detected transitions are D I $\text{Ly}\alpha$ and $\text{Ly}\beta$, offset by the appropriate $\delta v = -82\text{ km s}^{-1}$ from the hydrogen absorption.

To characterize the physical properties of these LLSs (summarized in Table 1), we modeled the hydrogen and deuterium absorptions using a χ^2 minimization algorithm (Table S1; Fig. S2 and S3, see SOM text 2) and we derived upper limits on the column densities of various ioniza-

tion states of heavy elements (Table S2; Fig. S4, see SOM text 3). To translate these limits into constraints on the gas metallicity, it is necessary to make assumptions on the ionization state of the gas (see SOM text 4). Every LLS with $N_{\text{HI}} \lesssim 10^{19} \text{ cm}^{-2}$ analyzed to date has exhibited absorption characteristic of a predominantly ionized gas (e.g. (12, 13)). Standard interpretation is that the medium has been photoionized by an external radiation field, presumably a combination of the extragalactic UV background (EUVB) generated by the cosmological population of quasars and galaxies together with emission from local sources (e.g. a nearby galaxy). This conclusion is based on comparison of the observed ionic column densities of heavy elements with simple photoionization models. Every previous LLS has shown substantial absorption from doubly and triply ionized species, e.g. Si^{++} and C^{+3} , which trace predominantly ionized gas. Parametrizing the ionization state in terms of the ionization parameter $U \equiv \Phi/(c n_{\text{H}})$, with Φ the flux of ionizing photons and n_{H} the gas volume density, all previously analyzed LLSs have exhibited $U \geq 10^{-3}$ corresponding to $n_{\text{H}} \leq 10^{-2} \text{ cm}^{-3}$ at $z \sim 3$ (Fig. S6).

Adopting this U value as a limit to the ionization state and current estimates for the spectral shape of the EUVB (14), we infer metallicities of $Z < 10^{-4.2} Z_{\odot}$ and $Z < 10^{-3.8} Z_{\odot}$ for LLS1134a and LLS0956B (see Fig. S5). These upper limits are 100 to 1000 times lower than typical measurements of LLSs and over an order of magnitude lower than any previous observed metallicity at $z > 2$ (Fig. 1). These limits are only comparable to the abundances detected in the most metal poor star (9) and are suggestive of a primordial composition. Super-solar metallicity is commonly found in the surroundings of quasars as well as in a few LLSs. Metallicities between solar and $\sim 1/10$ solar are typical of galaxies, and sub-solar metal enrichment down to $10^{-3} Z_{\odot}$ is characteristic of the ISM and IGM at early epochs. Remarkably, the most iron poor stars in the Galactic halo, thought to be the repository of the first generation of metals, have total heavy element abundance comparable to these limits, but generally above $\sim 1/1000$ solar. Our analysis uncovers regions of the universe at $z < 6$ with essentially primordial enrichment, whose traces can be found within the oldest stellar populations in the present universe (9).

The detection of deuterium in the metal free LLS1134a provides a direct confirmation of the BBN. From the analysis of the D and H absorption lines, we derive $\log(\text{D}/\text{H}) = -4.69 \pm 0.13$ (see SOM text 2). The observed value is consistent at 1σ with the theoretical predicted value $\log(\text{D}/\text{H}) = -4.592$ (15), assuming $\Omega_{b,0}$ from WMAP7. This measurement is in agreement with previous determinations in quasar absorption line systems at $z > 2$ (Table S3; Fig. 4). Because the lack of metals in LLS1134a confirms its pristine composition, this agreement strengthens the hypothesis that at low metallicities ($10^{-2} Z_{\odot}$ or less) the observed deuterium abundances are representative of the primordial value (16) and astration cannot be responsible for the lingering scatter in the observed D/H. Deuterium abundances from quasar absorption line systems are therefore solid anchor points for models of galactic chemical evolution (e.g. (17)). Combining D/H in LLS1134a with values from the known D-bearing systems, we obtain a logarithmic weighted mean $\log(\text{D}/\text{H}) = -4.556 \pm 0.034$ that translates into $\Omega_{b,0} h^2 (\text{BBN}) = 0.0213 \pm 0.0012$, after accounting for both random and systematic errors (3). Consistent with previous studies, we do not include in the weighted mean the error on the assumed level of the quasar continuum light.

The absence of metals in LLS1134a and LLS0956B is outstanding also in the framework of theories for the metal enrichment of cosmic structures (Fig. 5). Numerical simulations suggest that LLSs typically arise in galaxies (e.g. (18)), in dense gas above ~ 100 times the mean cosmic density ρ_{mean} . At the same time, in models of the IGM enrichment, metals are ejected to hundreds of kpc from star forming regions, resulting in substantial pollution of the nearby gas. As a consequence, the metallicity predicted for stars or for the ISM at $z < 4$ (19) ranges between $0.1 - 1 Z_{\odot}$, three orders of magnitude higher than the limits inferred for these two LLSs. Similarly, the metallicity predicted for the hot halo of galaxies and for the surrounding IGM (19, 20) exceeds by a factor of 10 or more the limits for LLS1134a and LLS0956B. Contrary to any prediction and any previous observation, these two LLSs reside at significant overdensity ($\rho/\rho_{\text{mean}} < 850$) but in an unpolluted portion of the universe.

Metallicity below $10^{-4} Z_{\odot}$ appears even exceptional when compared to the level of pre-enrichment from PopIII stars that is predicted by models (10, 21, 22) already 500 million years after the Big Bang ($z \sim 10$). Our limits place additional constraints on the widespread dispersal of metals from primordial stellar populations and the first generations of galaxies. Remarkably, the gas we detected could in principle fuel PopIII star-formation at $z \sim 3$, because its metallicity lies at or even below the minimum enrichment required for metal cooling to induce fragmentation in the collapsing material in the absence of dust (23). Given a lower limit on the LLS physical size $\ell = N_{\text{HI}}/(x_{\text{HI}}n_{\text{H}})$, with x_{HI} the neutral fraction and n_{H} the total hydrogen volume density, we can infer the total hydrogen mass in these clouds $M_{\text{H}} = m_{\text{p}}N_{\text{H}}\ell^2$. We find $M_{\text{H}} \gtrsim 6.2 \times 10^6 M_{\odot}$ for LLS1134a and $M_{\text{H}} \gtrsim 4.2 \times 10^5 M_{\odot}$ for LLS0956B, comparable to the mass of the mini-halos where the first generation of stars formed (e.g. (22)). Therefore, if this gas were able to collapse further and shield from the ambient UV radiation, it would potentially give rise to PopIII stars two billion years after the transition between the first and second generation of stars (PopII) is thought to have occurred. Thus, pair-production supernovae associated with the death of these massive and metal-free stars may be found even at modest redshifts (24).

The pristine composition of LLS1134a and LLS0956B can be reconciled with model predictions and previous observations if mixing of metals within the IGM is an inefficient and inhomogeneous process. A varying degree of metal enrichment is seen in multiple components of LLSs (12, 13, 25), implying that mixing does not operate effectively on small scales. The detection of ionized metals in LLS1134b, the weaker component at $+54 \text{ km s}^{-1}$ from LLS1134a, reinforces this point. Further, studies of metal systems in the low density and diffuse IGM suggest that at least some of the ionized heavy elements (e.g. C IV) are in small and short-lived clumps (26). A low volume filling factor for metals is also consistent with theories of metal ejection from supernovae, in which most of the heavy elements are initially confined in small bubbles (27) and only subsequently diffuse in the surrounding IGM. Plausibly, LLS1134a and LLS0956B originate in a filament of the cosmic web where primordial regions coexist with enriched pockets of gas. If the metal enrichment is highly inhomogeneous, these two LLSs could just be the tip of the iceberg of a much larger population of unpolluted absorbers that trace a large fraction of the dense IGM.

Beside the implications for the BBN and the metal distribution, the detection of metal free

LLSs is tantalizing in the context of galaxy formation and evolution. Modern theory and simulations predict that most of the gas that sustains star formation is accreted in galaxies through dense and narrow streams, known as cold flows (28,29). These gaseous filaments are highly ionized by both the EUVB and the radiation escaping from the central star forming regions. Cold flows should therefore appear as LLSs in the spectra of bright quasars (30–32). Further, in contrast to metal enriched gas that is outflowing from galaxies, this infalling material is expected to be metal poor (31). Although direct observational evidence of cold flows is still lacking, these streams are thought to be ubiquitous at high-redshift and primordial LLSs such as LLS1134a and LLS0956B are ideal candidates for this elusive mode of accretion.

References and Notes

1. E. M. Burbidge, G. R. Burbidge, W. A. Fowler, F. Hoyle, *Reviews of Modern Physics* **29**, 547 (1957).
2. J. M. O’Meara, *et al.*, *ApJL* **649**, L61 (2006).
3. M. Pettini, B. J. Zych, M. T. Murphy, A. Lewis, C. C. Steidel, *MNRAS* **391**, 1499 (2008).
4. E. Komatsu, *et al.*, *ApJS* **192**, 18 (2011).
5. J. X. Prochaska, E. Gawiser, A. M. Wolfe, S. Castro, S. G. Djorgovski, *ApJL* **595**, L9 (2003).
6. D. K. Erb, *et al.*, *ApJ* **644**, 813 (2006).
7. J. Schaye, *et al.*, *ApJ* **596**, 768 (2003).
8. R. A. Simcoe, W. L. W. Sargent, M. Rauch, *ApJ* **606**, 92 (2004).
9. E. Caffau, *et al.*, *Nature* **477**, 67 (2011).
10. J. Mackey, V. Bromm, L. Hernquist, *ApJ* **586**, 1 (2003).
11. J. H. Wise, T. Abel, *ApJ* **685**, 40 (2008).
12. G. E. Prochter, J. X. Prochaska, J. M. O’Meara, S. Burles, R. A. Bernstein, *ApJ* **708**, 1221 (2010).
13. J. X. Prochaska, S. M. Burles, *AJ* **117**, 1957 (1999).
14. F. Haardt, P. Madau, *arXiv:1105.2039* (2011).
15. G. Steigman, *Annual Review of Nuclear and Particle Science* **57**, 463 (2007).

16. D. Kirkman, D. Tytler, N. Suzuki, J. M. O’Meara, D. Lubin, *ApJS* **149**, 1 (2003).
17. D. Romano, M. Tosi, C. Chiappini, F. Matteucci, *MNRAS* **369**, 295 (2006).
18. K. Kohler, N. Y. Gnedin, *ApJ* **655**, 685 (2007).
19. B. D. Oppenheimer, R. Davé, N. Katz, J. A. Kollmeier, D. H. Weinberg, *arXiv:1106.1444* (2011).
20. L. Hernquist, V. Springel, *MNRAS* **341**, 1253 (2003).
21. N. Yoshida, V. Bromm, L. Hernquist, *ApJ* **605**, 579 (2004).
22. J. H. Wise, M. J. Turk, M. L. Norman, T. Abel, *arXiv:1011.2632* (2010).
23. V. Bromm, A. Ferrara, P. S. Coppi, R. B. Larson, *MNRAS* **328**, 969 (2001).
24. E. Scannapieco, P. Madau, S. Woosley, A. Heger, A. Ferrara, *ApJ* **633**, 1031 (2005).
25. V. D’Odorico, P. Petitjean, *A & A* **370**, 729 (2001).
26. J. Schaye, R. F. Carswell, T.-S. Kim, *MNRAS* **379**, 1169 (2007).
27. A. Ferrara, M. Pettini, Y. Shchekinov, *MNRAS* **319**, 539 (2000).
28. D. Kereš, N. Katz, D. H. Weinberg, R. Davé, *MNRAS* **363**, 2 (2005).
29. A. Dekel, *et al.*, *Nature* **457**, 451 (2009).
30. C.-A. Faucher-Giguère, D. Kereš, *MNRAS* **412**, L118 (2011).
31. M. Fumagalli, *et al.*, *MNRAS* pp. 1589–+ (2011).
32. F. van de Voort, J. Schaye, G. Altay, T. Theuns, *arXiv:1109.5700* (2011).
33. R. Schneider, A. Ferrara, P. Natarajan, K. Omukai, *ApJ* **571**, 30 (2002).
34. R. Davé, K. Finlator, B. D. Oppenheimer, *arXiv:1108.0426* (2011).
35. J. M. O’Meara, *et al.*, *ApJ* **656**, 666 (2007).
36. S. S. Vogt, *et al.*, *Society of Photo-Optical Instrumentation Engineers (SPIE) Conference Series*, D. L. Crawford & E. R. Craine, ed. (1994), vol. 2198 of *Society of Photo-Optical Instrumentation Engineers (SPIE) Conference Series*, pp. 362–+.
37. J. B. Oke, *et al.*, *PASP* **107**, 375 (1995).
38. C. C. Steidel, *ApJS* **74**, 37 (1990).

39. B. D. Savage, K. R. Sembach, *ApJ* **379**, 245 (1991).
40. A. Lidz, *et al.*, *ApJ* **718**, 199 (2010).
41. F. Haardt, P. Madau, *ApJ* **461**, 20 (1996).
42. M. Rauch, *et al.*, *ApJ* **489**, 7 (1997).
43. G. J. Ferland, *et al.*, *PASP* **110**, 761 (1998).
44. M. Asplund, N. Grevesse, A. J. Sauval, P. Scott, *ARAA* **47**, 481 (2009).
45. O. Gnat, A. Sternberg, *ApJS* **168**, 213 (2007).
46. A. Aguirre, C. Dow-Hygelund, J. Schaye, T. Theuns, *ApJ* **689**, 851 (2008).
47. J. X. Prochaska, *et al.*, *ApJL* **648**, L97 (2006).
48. J. X. Prochaska, *ApJL* **511**, L71 (1999).
49. J. M. O’Meara, *et al.*, *ApJ* **552**, 718 (2001).
50. S. Burles, D. Tytler, *ApJ* **507**, 732 (1998).
51. S. Burles, D. Tytler, *ApJ* **499**, 699 (1998).
52. D. Kirkman, D. Tytler, S. Burles, D. Lubin, J. M. O’Meara, *ApJ* **529**, 655 (2000).
53. N. H. M. Crighton, J. K. Webb, A. Ortiz-Gil, A. Fernández-Soto, *MNRAS* **355**, 1042 (2004).
54. S. A. Levshakov, I. I. Agafonova, M. Centurión, P. Molaro, *A & A* **397**, 851 (2003).
55. D. Reimers, S. Vogel, *A & A* **276**, L13+ (1993).
56. W. L. W. Sargent, C. C. Steidel, A. Boksenberg, *ApJ* **351**, 364 (1990).
57. S. A. Levshakov, I. I. Agafonova, S. D’Odorico, A. M. Wolfe, M. Dessauges-Zavadsky, *ApJ* **582**, 596 (2003).
58. L. Spitzer, *Physical processes in the interstellar medium* (New York Wiley-Interscience, 1978. 333 p., 1978).
59. R. A. Jorgenson, A. M. Wolfe, J. X. Prochaska, *ApJ* **722**, 460 (2010).
60. B. E. Penprase, J. X. Prochaska, W. L. W. Sargent, I. Toro-Martinez, D. J. Beeler, *ApJ* **721**, 1 (2010).
61. J. X. Prochaska, H.-W. Chen, M. Dessauges-Zavadsky, J. S. Bloom, *ApJ* **666**, 267 (2007).

- 62. F. Mannucci, *et al.*, *MNRAS* **398**, 1915 (2009).
- 63. D. E. Osterbrock, *Astrophysics of gaseous nebulae and active galactic nuclei* (University Science Books, Mill Valley, CA, 1989, 1989).
- 64. D. Fabbian, P. E. Nissen, M. Asplund, M. Pettini, C. Akerman, *A & A* **500**, 1143 (2009).
- 65. T. Suda, *et al.*, *MNRAS* **412**, 843 (2011).
- 66. D. C. Morton, *ApJS* **149**, 205 (2003).
- 67. M. Pettini, D. V. Bowen, *ApJ* **560**, 41 (2001).
- 68. M. Pettini, B. J. Zych, C. C. Steidel, F. H. Chaffee, *MNRAS* **385**, 2011 (2008).
- 69. We thank A. Aguirre, N. Lehner, and P. Madau for providing comments on this manuscript. We would like to thank the MPIA at Heidelberg for their hospitality. J.X.P. acknowledges support from the Humboldt Foundation. Support for this work came from NSF grant AST0548180. We acknowledge the use of VPFIT. This work is based on observations made at the W. M. Keck Observatory, which is operated as a scientific partnership among the California Institute of Technology, the University of California and NASA. The Observatory was made possible by the generous financial support of the W. M. Keck Foundation. The authors wish to recognize and acknowledge the very significant cultural role and reverence that the summit of Mauna Kea has always had within the indigenous Hawaiian community. We are most fortunate to have the opportunity to conduct observations from this mountain. The data reported in this paper are available through the Keck Observatory Archive (KOA).

Supporting Online Material

www.sciencemag.org

Supporting text

Tables S1-S3

Figures S1-S6

References (35-68)

	LLS1134a	LLS0956B
Redshift	3.410883 ± 0.000004	3.096221 ± 0.000009
$\log N_{\text{HI}}$	17.95 ± 0.05	17.18 ± 0.04
$\log \text{D}/\text{H}$	-4.69 ± 0.13^a	-
$b_{\text{HI}} \text{ (km s}^{-1}\text{)}$	15.4 ± 0.3	20.2 ± 0.8
Temperature (K)	$< (1.43 \pm 0.05) \times 10^4$	$< (2.48 \pm 0.19) \times 10^4$
Metallicity (Z_{\odot})	$< 10^{-4.2}$	$< 10^{-3.8}$
$\log x_{\text{HI}}$	< -2.10	< -2.40
$\log n_{\text{H}}$	< -1.86	< -1.98
$\log U^b$	> -3	> -3

^a Including LLS1134a, the current best estimate for the primordial deuterium abundance becomes $\log(\text{D}/\text{H}) = -4.556 \pm 0.034$. ^b The listed values are physically motivated, but not directly measured. Note that the metallicity, x_{HI} , and n_{H} depend on the assumed value.

Table 1: Summary of the physical properties for LLS1134a and LLS0956B. For each system, we present: redshift, the hydrogen column density (N_{HI}), the deuterium abundance (D/H), the Doppler parameter (b_{HI}), the temperature, the metallicity, the hydrogen neutral fraction (x_{HI}), the total hydrogen volume density (n_{H}), and the ionization parameter (U).

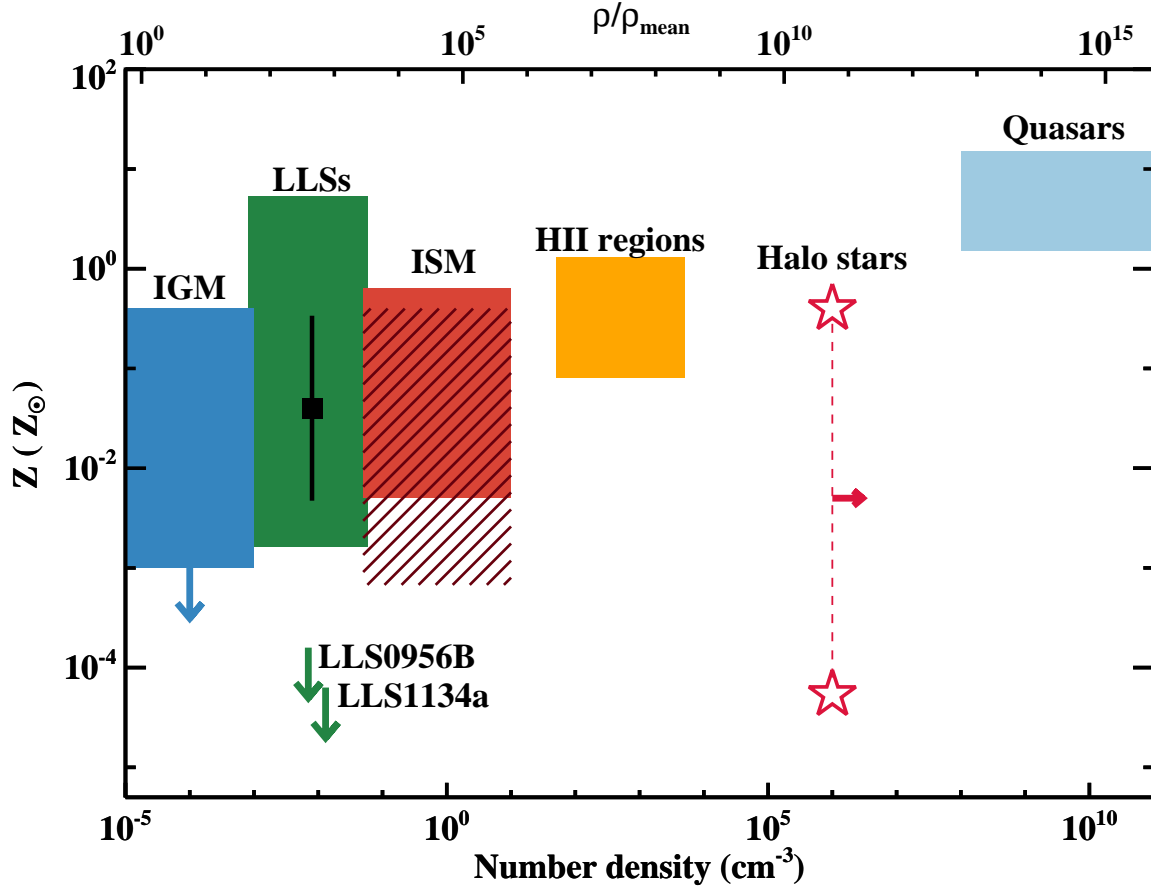


Figure 1: Peak to peak variation of the observed metallicity in $z \gtrsim 2$ cosmic structures at different densities. The blue, green and red rectangles show the spread in observed metallicities for diffuse gas in the universe; respectively, these are the IGM, LLSs, and galactic ISM. Orange rectangle: H II regions in galaxies. Light blue rectangle: quasar broad line regions. The black point with error bars marks the mean metallicity and the standard deviation for $z > 1.5$ LLSs. Galactic halo stars (stars connected with a dashed line) are represented at arbitrary density for visualization purposes. The top axis translates the number density in the overdensity above the mean baryon cosmic density at $z = 3.5$. The upper limits on the metallicity for LLS1134a and LLS0956B are shown with green arrows, assuming $\log U = -3$. Higher ionization parameters would shift these limits to lower densities and lower metallicity. See the SOM text 5 for additional details on the observations presented in this figure.

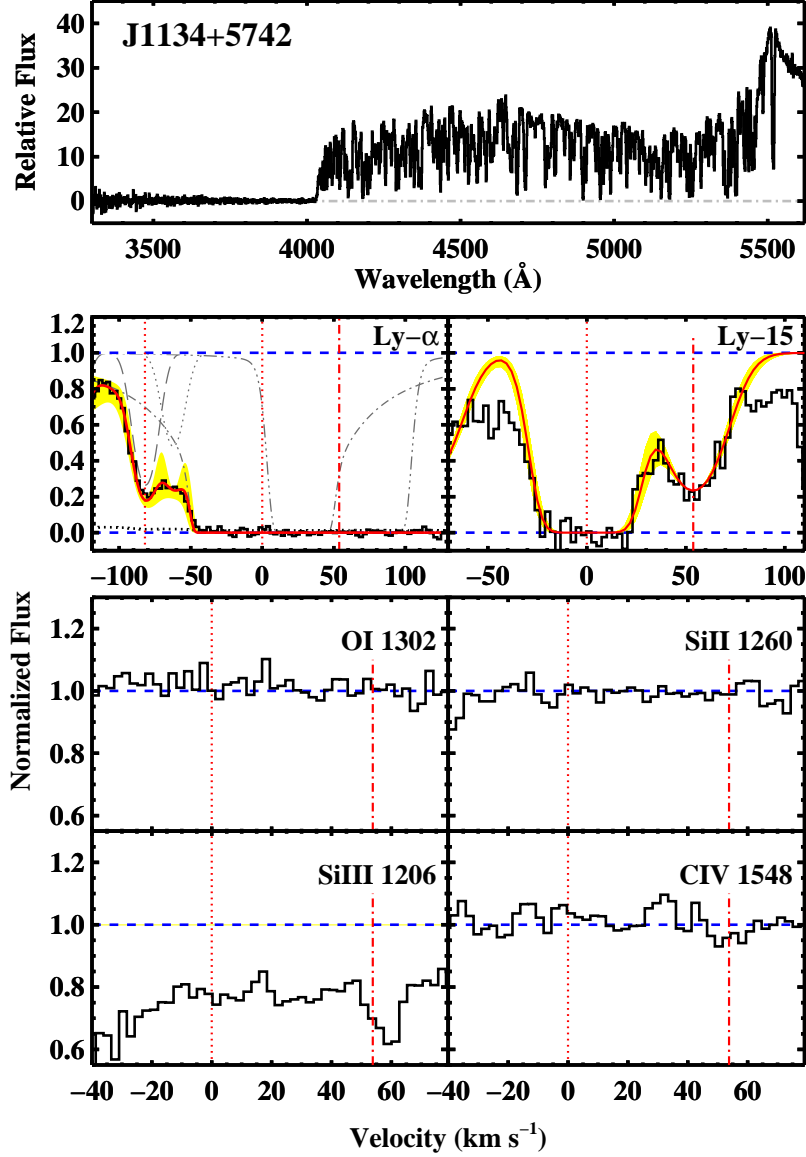


Figure 2: Top panel: Keck/LRIS spectrum of the QSO J1134+5742. A LLS at $z \sim 3.4$ is clearly visible from the break at ~ 4000 Å. Middle panels: H I Lyman series transitions in the LLS1134a. Superimposed to the data are the best-fit model (red line) and the 2σ errors (yellow shaded regions). Individual components included in the model are marked with thin gray lines and the position of the hydrogen and deuterium are indicated by vertical dotted lines. The second hydrogen component (LLS1134b) at $+54$ km s $^{-1}$ is marked with a dash-dotted line. Bottom panels: selected strong metal-line transitions in LLS1134a (dotted lines) and LLS1134b (dash-dotted lines). Unrelated absorption from the IGM contaminates the Si III transition (see Fig. S4).

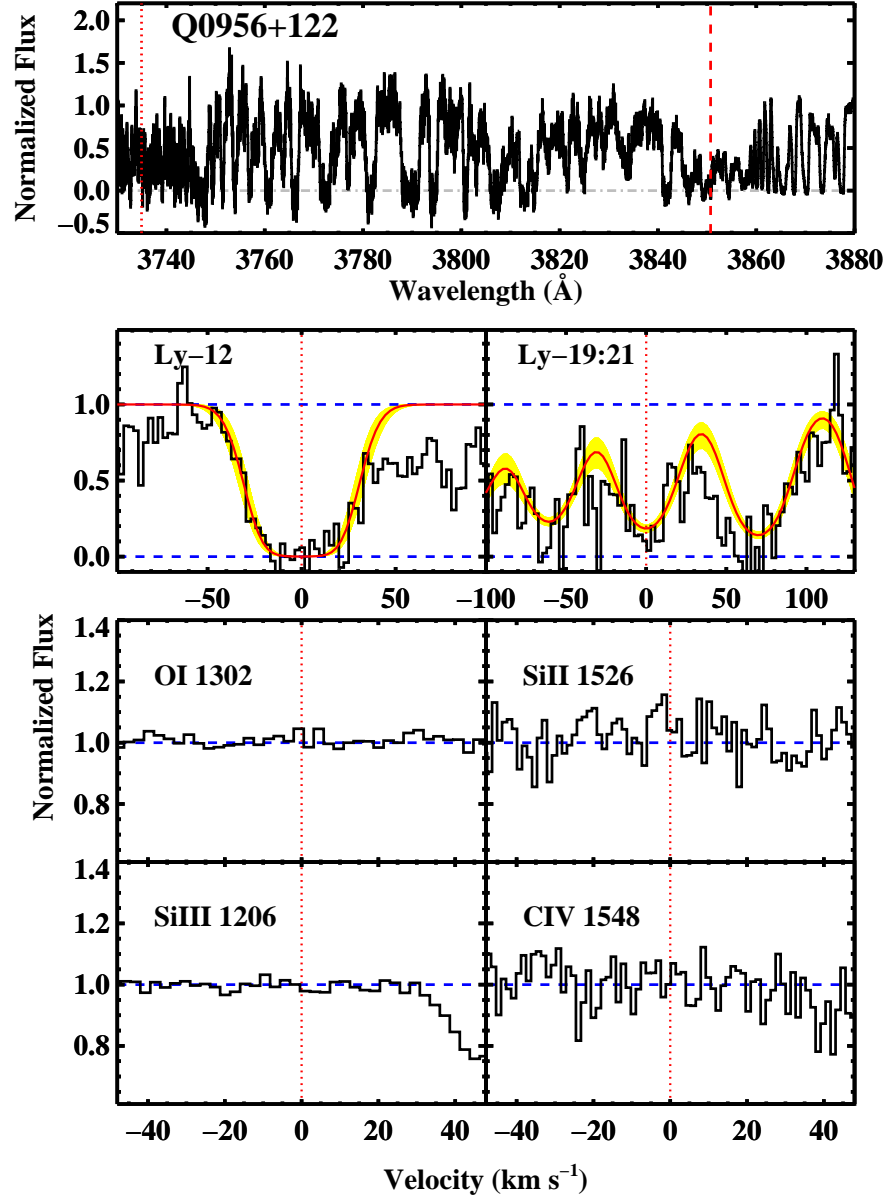


Figure 3: Top panel: Keck/HIRES spectrum of the QSO Q0956 + 122. The flux decrements at ~ 3860 Å and ~ 3750 Å reveal two partial LLSs at $z \sim 3.22$ (LLS0956A) and $z \sim 3.10$ (LLS0956B). The corresponding Lyman limits are marked with vertical lines. Middle panels: hydrogen Lyman series transitions for LLS0956B shown relative to $z = 3.096221$. Superimposed to the data, the best-fit model (red lines) and 2σ uncertainties (yellow shaded regions). Bottom panels: selected strong metal-line transitions for LLS0956B.

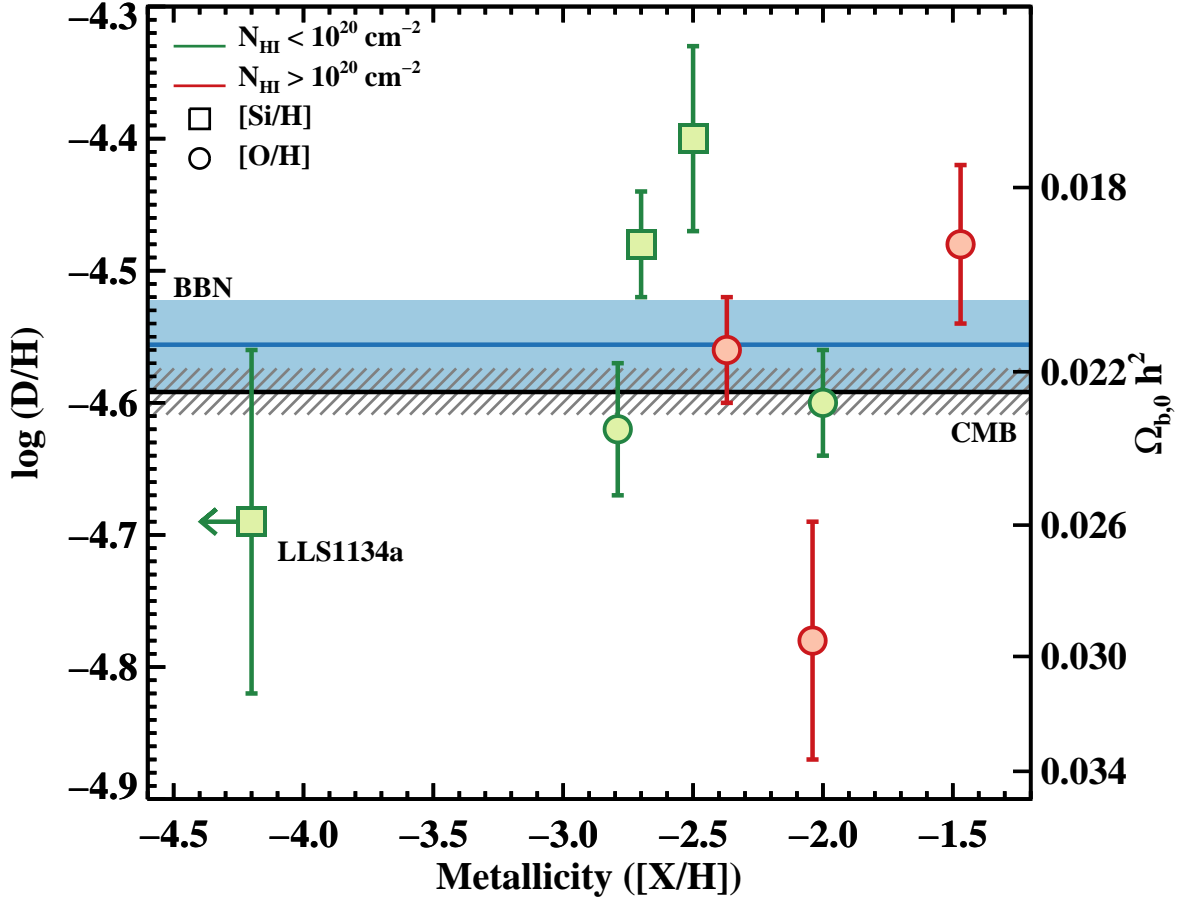


Figure 4: Deuterium abundances as a function of metallicity ($[X/H] \equiv \log(X/H) - \log(X/H)_{\odot}$) for the $z > 2$ absorption line systems. Green symbols are for LLSs, while red symbols are for higher column density absorbers ($N_{\text{HI}} > 10^{20} \text{ cm}^{-2}$). Metallicities obtained with silicon are indicated by squares, while those obtained with oxygen are indicated with circles. The right-hand axis translates the deuterium abundance to the cosmic baryon density $\Omega_{b,0} h^2$. The inferred $\Omega_{b,0} h^2$ (BBN) is shown with a solid blue line, together with the 1σ errors (light blue shaded area). The CMB value and 1σ errors from WMAP7 are instead shown with a solid black line and a gray dashed area.

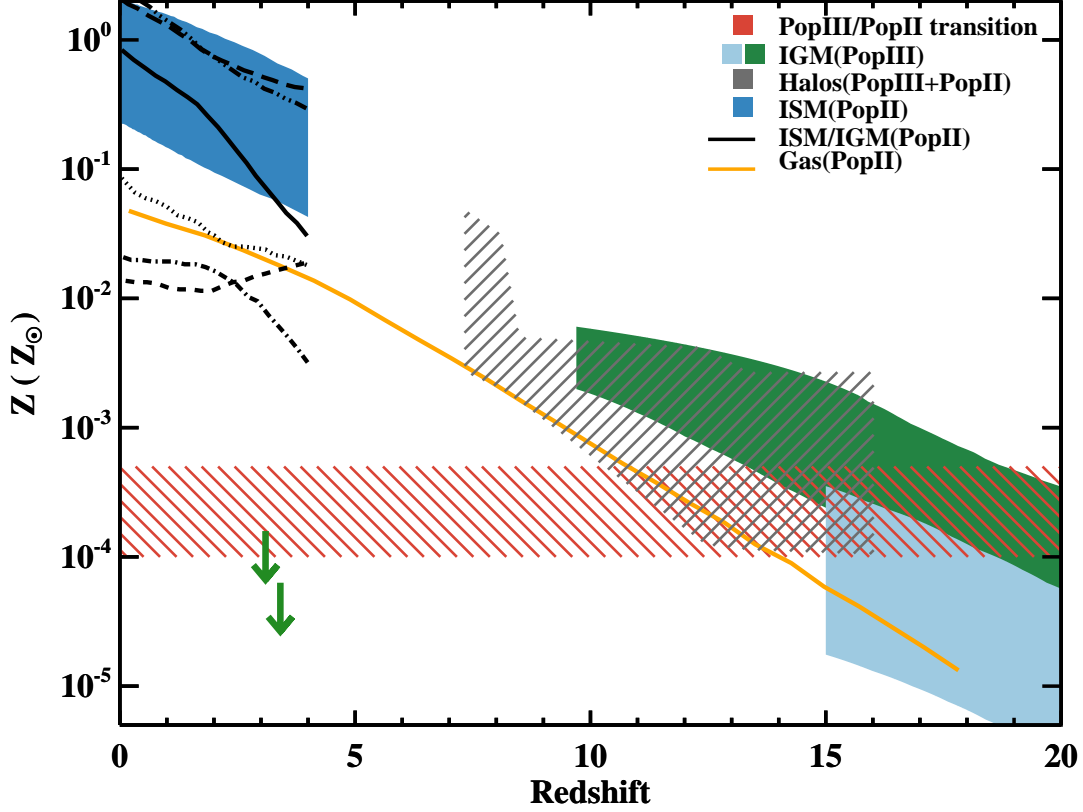


Figure 5: Overview of analytic models and simulations for the metal enrichment of the universe. Light blue and green shaded regions: IGM metallicity from PopIII stars with mixing between 1 – 0.05 and different star formation histories (10, 21). Red dashed region: critical metallicity that marks the transition between PopIII and PopII stars (23, 33). Orange line: analytic model for the gas metal content in the universe from PopII stars and galactic winds (20). Gray shaded region: gas metallicity within halos from hydrodynamical simulations that include yields from both PopIII and PopII stars (22). Blue shaded region: analytic model for the ISM metallicity at different halo masses ($10^{11} - 10^{14} M_{\odot}$) and different wind models (34). Black lines: metallicity from hydrodynamical simulations with momentum driven winds (19) in condensed gas (solid line), hot halo (dotted line), warm-hot intergalactic medium (dashed line), diffuse gas (dash-dotted line), ISM (dash-triple-dotted line), and stars (long-dashed line). Upper limits on the metallicities of LLS1134a and LLS0956B are marked with green arrows.

Supporting Online Material

1 Observations and Data Reduction

Previous spectra of quasars SDSS J113418.96+574204.6 and Q0956 + 122 had shown substantial absorption at wavelengths $\lambda < 4000\text{\AA}$ characteristic of the continuum opacity of H I gas. LLS1134a and LLS0956B were identified as part of an ongoing program to explore the incidence and physical characteristics of LLSs (12, 35) from a sample of ~ 50 absorbers, many of which have apparently low metallicity ($< 1/100$ solar).

We first observed quasar J1134+5742 on UT January 5, 2006 with the HIRES spectrometer (36) on the Keck I telescope on Mauna Kea. The data were obtained in two exposures totaling 6300 seconds, with the instrument configured with the red cross-disperser, the C5 decker, and the kv380 blocking filter to suppress second order flux. In this configuration, the instrument provides a resolution of $\sim 8 \text{ km s}^{-1}$ FWHM, and the echelle and cross-disperser angles were set to provide wavelength coverage $4017 \text{\AA} < \lambda < 8534 \text{\AA}$. These spectra have gaps in coverage at $\lambda \sim 5450\text{\AA}$ and 7050\AA due to spacings between the CCDs in the detector mosaic. There are also a series of gaps in wavelength coverage beyond $\lambda > 6300\text{\AA}$ where the free spectral range of the spectrometer exceeds the detector width.

We observed Q0956 + 122 with HIRES once on UT January 3, 2006 for 7200 seconds, and again on UT April 7, 2006 for 1800 seconds. For the January data, HIRES was configured with the UV cross-disperser and the C5 decker, again providing $\sim 8 \text{ km s}^{-1}$ FWHM resolution. The wavelengths covered in this configuration were $3621 \text{\AA} < \lambda < 5533 \text{\AA}$, with gaps in coverage only related to the CCD mosaic. The April 2006 data had HIRES configured with the red cross-disperse, the C1 Decker, and the og530 blocking filter. The wavelengths $5465 \text{\AA} < \lambda < 9998 \text{\AA}$ were covered with wavelength gaps due to the spacings of the CCD mosaic and the limited detector size.

For both quasars, the 2D images were reduced with the HIRESredux pipeline¹ which extracts and coadds the data. An interactive continuum fitting procedure within the pipeline assigns a continuum level to each coadded spectral order, and the continuum normalized spectra are then combined into a single 1D spectrum. For J1134+5742, the resultant 1D spectrum has a signal-to-noise ratio $S/N \sim 25$ per 2.6 km s^{-1} pixel at 6300\AA , the central wavelength. For Q0956 + 122, the 1D spectra have $S/N \sim 30$ per 2.6 km s^{-1} pixel at 4500\AA for the UV cross-disperser data, and ~ 10 per 1.4 km s^{-1} pixel at 6000\AA for the red cross-disperser data.

We also observed J1134+5742 on UT 2011 July 1 with the LRIS spectrograph (37) on the Keck I telescope on Mauna Kea. We obtained a single exposure of 400 seconds, with the instrument configured with the 600/4000 grism, the D560 dichroic and the 600/7500 grating, tilted to ensure continuous spectral coverage between the blue and red arms. The 2D images were reduced with the LowRedux pipeline² which calibrates and extracts the data.

¹<http://www.ucolick.org/~xavier/HIRedux/index.html>

²<http://www.ucolick.org/~xavier/LowRedux/index.html>

2 Hydrogen and Deuterium Analysis

We now describe the H I and D I analysis for each LLS.

2.1 The Lyman Limit System at $z = 3.410883$ toward J1134+5742

Both the strong Lyman limit absorption visible in the Keck/LRIS spectrum (Fig. 2), and the saturation of the high-order Lyman series lines in the Keck/HIRES data (Fig. S2) imply a large H I column density, N_{HI} . Fig. S1 shows a zoom-in of the Keck/LRIS spectrum for J1134+5742, focusing on the Lyman limit absorption. We estimate the flux just redward of the Lyman limit to be 13 ± 2 in our relative units. This estimate appropriately includes the attenuation of the quasar light by the $\text{Ly}\alpha$ forest. In the following, we assume a flat spectrum for the continuum and note that a more realistic spectrum would yield a slightly higher estimate for the N_{HI} value. Just blueward of the Lyman limit ($\lambda = 3950 - 4000\text{\AA}$), we set a conservative upper limit to the relative flux of 0.05. Combining these two measurements, we estimate a lower limit to the optical depth at the Lyman limit of $\tau_{\text{LL}} > \ln(9./0.05) > 5$ for a total $N_{\text{HI}} > 10^{17.9} \text{ cm}^{-2}$. The model for this N_{HI} limit, shown as the green line in Fig. S1, is marginally acceptable at $\lambda \sim 4000\text{\AA}$, but predicts a recovery of the flux at $\lambda < 3800\text{\AA}$ that appears inconsistent with the observations. Metal-lines and strong $\text{Ly}\alpha$ lines in the HIRES spectrum, however, reveal the presence of other absorbers along the sightline to J1134+5742 at redshifts $z = 3.0283$, $z = 3.0753$, $z = 3.1047$, $z = 3.2396$, $z = 3.2616$, and $z = 3.3223$. These systems could contribute to the opacity at $\lambda < 3942\text{\AA}$. If they do not, then LLS1134a must have a higher N_{HI} value.

Fig. S1 shows the data binned with a weighted mean in windows of 50\AA between $3400 - 4000\text{\AA}$. Overplotted on these binned evaluations (whose errors only reflect statistical uncertainty) is a model curve for $N_{\text{HI}} = 10^{18.05} \text{ cm}^{-2}$ (blue line). This N_{HI} value reproduces the observed absorption to $\sim 3400\text{\AA}$. Larger N_{HI} values are not ruled out by the analysis, especially when one allows for systematic error (e.g. sky subtraction). In summary, we report a lower limit to the total N_{HI} value of $10^{17.9} \text{ cm}^{-2}$ and note the data require yet higher values if LLS1134a dominates the opacity at $\lambda < 3700\text{\AA}$.

To further refine the N_{HI} measurement and its redshift distribution, we have performed detailed analysis of the Lyman series lines. This analysis, however, is challenged by the fact that gas with $N_{\text{HI}} \sim 10^{18} \text{ cm}^{-2}$ has Lyman series lines that lie on the saturated portion of the curve-of-growth (e.g. (12)). As such, we proceed cautiously as this may impose large uncertainties in the model. We may first set a strict upper limit to the total N_{HI} of LLS1134a from the absence of substantial damping wings in the $\text{Ly}\alpha$ profile (Fig. 2). Because the flux would be over-absorbed for all models with N_{HI} exceeding $10^{18.7} \text{ cm}^{-2}$, this is the largest N_{HI} value allowed for LLS1134a. Second, the complete absorption at $\lambda \sim 4030\text{\AA}$ by the Lyman series requires $N_{\text{HI}} > 10^{17.6} \text{ cm}^{-2}$, consistent with the Lyman limit analysis performed above.

Lastly, we can model the H I absorption using the VPFIT v9.5 package that allows one to fit multiple Voigt profiles to the spectrum. Our general approach is to include as few components as

possible (each defined by a redshift z , column density N_{HI} , and Doppler parameter b_{HI}) to match the Lyman series absorption. The data are best described by two principal H I components (LLS1134a and LLS1134b), as evident from a visual inspection of the higher order Lyman series lines (Fig. 2 and S2). Since LLS1134b is unsaturated beyond Ly-14, we first measure the line-parameters of this subsystem using the Lyman series lines between Ly-10 and Ly-16. We find $z = 3.41167 \pm 0.00001$, $b_{\text{HI}} = 18.0 \pm 0.9 \text{ km s}^{-1}$ and $\log N_{\text{HI}} = 16.71 \pm 0.02$ indicating that this component has a nearly negligible contribution to the observed Lyman limit. Adding an additional uncertainty of 0.02 dex related to the 1–3% error in the continuum placement, our best fit value for the column density of LLS1134b becomes $\log N_{\text{HI}} = 16.71 \pm 0.03$. Then, we model LLS1134a and the deuterium absorption, using both high order Lyman series lines (Ly-7 through Ly-16) as well as Ly- α and Ly- β . For these transitions, we must include absorption from gas unrelated to LLS1134 which we ascribe to coincident Ly α absorption from lower redshift absorbers. A summary of the model parameters is given in Table S1.

The strongest H I component has $z = 3.410883 \pm 0.000004$, $\log N_{\text{HI}} = 17.94 \pm 0.05$ and an H I Doppler parameter $b_{\text{HI}} = 15.4 \pm 0.3 \text{ km s}^{-1}$. The latter is consistent with a predominantly ionized gas at a temperature $T \leq 1.4 \times 10^4 \text{ K}$. The line-parameters for LLS1134a are well constrained by the full Lyman series and the resultant N_{HI} value is consistent with our Lyman limit analysis of the Keck/LRIS spectrum. Despite the line-saturation, there is substantial constraint on the b_{HI} value, and thereby the N_{HI} value, from the line-profile shapes of the Lyman series lines. This conclusion hinges, however, on the assumption that the H I absorption at $z \sim 3.41088$ is dominated by a single component. As we will demonstrate in the next paragraph, this assumption is well supported by the analysis of neighboring D I absorption. From the above discussion, we conclude $N_{\text{HI}} = 10^{17.95 \pm 0.05} \text{ cm}^{-2}$ for LLS1134a. The 0.02 dex error on the continuum placement is in this case negligible compared to the statistical uncertainty. In regards to the metallicity of this gas, we further emphasize that $\log N_{\text{HI}} \geq 17.95$ is preferred by the analysis of the Lyman continuum opacity, despite the symmetric statistical error. If anything, metallicity limits derived from this N_{HI} value may be considered conservative.

In addition to the H I Lyman series, LLS1134a exhibits substantial absorption for the D I Ly α and Ly β transitions at the expected -82 km s^{-1} offset from the H I lines. Due to blending with absorption lines from lower redshift gas, deuterium is not detected in the remaining Lyman series lines. Although both of the D I transitions are partially blended with (presumed) H I absorption, a simultaneous fit to the hydrogen and deuterium absorption lines (Fig. S2) constrains $\log N_{\text{DI}} = 13.26 \pm 0.04$ and $b_{\text{DI}} = 10.2 \pm 0.8$. The latter parameter is fully consistent with the b_{HI} value derived from the hydrogen absorption. The deuterium estimate is more sensitive to the continuum placement error than hydrogen, particularly at the position of Ly- β . Therefore, we include an additional uncertainty of ~ 0.08 dex, computed by repeating multiple times this analysis after having varied the continuum level by $\pm 1 - 3\%$. When we express the Doppler parameter as a function of thermal broadening b_{ther} and turbulent component b_{turb} , the expected ratio of the hydrogen and deuterium b parameters is $b_{\text{DI}}/b_{\text{HI}} = \sqrt{1 - 0.5\phi}$ with $\phi = b_{\text{HI,ther}}^2 / (b_{\text{HI,ther}}^2 + b_{\text{turb}}^2)$ and $0 < \phi < 1$. The measured $b_{\text{DI}}/b_{\text{HI}} = 0.66$ is within 10% of the expected value for turbulent broadening ($\phi \sim 1$). The best-fit D/H ratio for LLS1134a

is $\log(D/H) = -4.69 \pm 0.06$, in agreement with previous determinations (Table S3). This consistency provides additional confidence on the model for the hydrogen absorption. Due to the partial blending of the D I lines with intervening hydrogen, the deuterium column density is affected by the additional uncertainty on the line parameters for the hydrogen absorption. Including this error, our best estimate becomes $\log(D/H) = -4.69 \pm 0.09$. Finally, including the uncertainty on the continuum determination, we find $\log(D/H) = -4.69 \pm 0.13$.

2.2 The Lyman Limit System at $z = 3.096221$ toward Q0956 + 122

A partial LLS (LLS0956A) was previously identified in low-resolution spectra of Q0956 + 122 and associated with corresponding metal-line absorption at $z = 3.2228$ (38). We confirm this identification (Fig. 3). An LLS at lower redshift was also reported by Steidel et al. (38), who proposed it was associated with a metal-line system at $z = 3.1142$. Our analysis of the HIRES spectra, however, only reveals substantial high-order Lyman series absorption for a system at $z \sim 3.096$ and we adopt this as the redshift for LLS0956B.

Non-zero flux is detected blueward of the Lyman limit for each system, implying $N_{\text{HI}} < 10^{17.8} \text{ cm}^{-2}$ for both LLS0956A and LLS0956B. At this optical depth ($\tau_{\text{LL}} \sim 1$), the total N_{HI} value is well established by the Lyman limit opacity and the analysis of unsaturated Lyman series lines.

The hydrogen Lyman series of LLS0956A is detected through to Lyman-21 in our HIRES data, together with C IV and Si IV metal lines. By modeling the unsaturated hydrogen transitions from Lyman-16 to Lyman-21, we derive the redshift $z = 3.223194 \pm 0.000002$, the column density $\log N_{\text{HI}} = 17.37 \pm 0.01$, and the Doppler parameter $b_{\text{HI}} = 20.4 \pm 0.2$. Similarly, for LLS0956B, the hydrogen Lyman series is clearly visible through to Lyman-15 and, at lower signal-to-noise, through to Lyman-21. No other metal lines are detected at the hydrogen position, while deuterium is blended in the strongest transitions. Combining both high-order saturated and non-saturated H I absorption lines, we model this LLS with a single component at $z = 3.096221 \pm 0.000009$, with $b_{\text{HI}} = 20.2 \pm 0.8 \text{ km s}^{-1}$ and $\log N_{\text{HI}} = 17.18 \pm 0.03$ (Fig. 3 and S3). After accounting for an additional 0.02 dex of uncertainty on the continuum placement, the best fit column density for LLS0956B becomes $\log N_{\text{HI}} = 17.18 \pm 0.04$. The Doppler parameter implies a temperature $T \leq 2.5 \times 10^4 \text{ K}$, typical for photoionized gas.

3 Metal Line Analysis

We now discuss upper limits to the column densities of atoms and ions for heavy elements in these metal free LLSs.

3.1 LLS1134

LLS1134a is conspicuously free of metal-line absorption, as shown in Fig. 2 where we mark for selected ionic transitions the position corresponding to this LLS and to the weaker hydrogen component ($z = 3.410883$ and $z = 3.41167$ respectively). For both LLS1134a and LLS1134b, we can place upper limits to the ionic column densities using the apparent optical depth method (39), with the key limiting factors being the S/N of the spectrum and contamination from the Ly α forest (i.e. Ly α lines at unrelated wavelengths). For this analysis, we choose a velocity window of $\pm 15 \text{ km s}^{-1}$ that is wide enough to encompass the expected width for metal lines given the hydrogen and deuterium absorption properties. A larger velocity window of $\pm 20 \text{ km s}^{-1}$ would yield slightly higher (~ 0.06 dex) limits. A summary of the metal column densities is presented in Table S2.

For most of the listed ionic transitions, we place robust upper limits based solely on the variance and the uncertainty associated with a $1 - 3\%$ (S/N dependent) error in continuum placement. Transitions blueward of 5450\AA , however, lie within the Ly α forest which complicates the estimates. Of particular interest to the metallicity of LLS1134a are the strong transitions of Si III 1206 and C III 977. Fig. S4 reveals that there is substantial absorption at the predicted wavelength for each transition. This absorption is broad, however, and has peak optical depth that is substantially offset from the predicted line-center. It is certain, therefore, that these transitions are blended with coincident absorption by the IGM. In this case, an upper limit based on the apparent optical depth would overestimate the column densities.

Better limits to the Si III and C III column densities can be derived using models for these absorption lines. We fix the Doppler parameters for the metal lines using the hydrogen and deuterium b values. From the H I and D I lines, we infer a temperature $(1.6 \pm 0.2) \times 10^4 \text{ K}$ and an upper limit on the turbulent velocity $b_{\text{turb}} < 2.2 \text{ km s}^{-1}$. Carbon and silicon absorption lines that arise in gas with these properties would be characterized by $b_{\text{C}} = 6.9 \text{ km s}^{-1}$ and $b_{\text{Si}} = 5.3 \text{ km s}^{-1}$. These Doppler parameters are within the range commonly observed for metal-line transitions (e.g. (40)). A first limit to the column densities of C III and Si III is set by demanding that the peak optical depth of each metal line does not exceed the observed absorption. This approach, that basically ignores the fact that the opacity is dominated by coincident IGM lines, yields upper limits of $\log N_{\text{SiIII}} < 11.85$ and $\log N_{\text{CIII}} < 12.45$. Lines of column density higher than these would exceed the observed absorption at the corresponding transitions, as shown in the top panels of Fig. S4.

A substantial fraction of the opacity at the Si III and C III frequencies must however arise from the two broad Ly α forest lines blueward to these metal transitions. We set therefore limits to $\log N_{\text{SiIII}}$ and $\log N_{\text{CIII}}$ using a two component model that includes both the metal lines and the Ly α forest. Following this procedure, we find $\log N_{\text{SiIII}} < 11.40$ and $\log N_{\text{CIII}} < 12.20$. Since additional Ly α lines at both negative and positive velocities are required to account for all the observed absorption, the choice of this minimal scenario (only two components) yields a quite conservative limit to the metal column densities.

Inspecting the strongest transitions of LLS1134b, the second main hydrogen component at

$z = 3.41167$, we see that Si III and C III are detected. These transitions are commonly found in highly ionized LLSs. Again using the apparent optical depth method, we find for the column densities of these ions $\log N_{\text{CIII}} = 13.03 \pm 0.02$ and $\log N_{\text{SiIII}} = 12.15 \pm 0.02$. While a strong line is clearly visible at the position of S III for this component, the implied column density would greatly exceed that for Si III and C III indicating that the absorption is dominated by contamination from the Ly α forest.

3.2 LLS0956B

Similarly to LLS1134a, LLS0956B is free of metal line absorption (Fig. 3). Using the apparent optical depth method, we determine upper limits to the ionic column densities in the velocity interval $\pm 15 \text{ km s}^{-1}$, consistent with the expected metal line width. The metal column densities for the strongest transitions, including the variance and uncertainty related to continuum placement, are listed in Table S2.

C III $\lambda 977$ is blended in the Ly α forest. Supported by the lack of any silicon absorption (Si II, Si III, and Si IV) and the absence of C II and C IV, we conclude that carbon is not present in this system to limits comparable to the ones inferred from silicon. Therefore, we do not include C III $\lambda 977$ in our estimates of the metallicity, but we rely on the Si III upper limit which we measure directly with the apparent optical depth method. We note that a larger velocity window of $\pm 20 \text{ km s}^{-1}$ would result in a slightly higher (0.06 dex) column density limit. We also note that the strongest Si II line at $\lambda 1260$ is overwhelmingly contaminated by intervening H I absorption and we use the Si II $\lambda 1526$ line to set a limit for this ion.

4 Metallicity Limits

Having established the H I column densities and limits to the ionic column densities of Si, C, and O, we may set upper limits to the heavy element abundances in the two LLSs. This requires, however, a careful consideration of the ionization state of the gas. Generally, the ionization state is assessed through a comparison of observed ionic column densities with ionization models. Absent the detection of *any* metal transitions, we must consider physically-motivated scenarios for the properties of the gas and thereby estimate limits to the metallicities.

In a perfectly neutral medium, all of the elements would be in their atomic state (ignoring molecular formation) and one could estimate the metallicity directly from the observed column densities of the atomic transitions (e.g. H I, C I, O I). In this extreme model one would recover $\log(\text{O}/\text{H}) - \log(\text{O}/\text{H})_{\odot} \equiv [\text{O}/\text{H}] < -1.9(-1.4)$ and $[\text{C}/\text{H}] < -2.1(-1.3)$ for LLS1134a (LLS0956B), which are the most conservative limits possible. In essentially all astrophysical environments, however, the gas is irradiated by local and external sources which photoionizes at least the outer layers of the cloud. Photons with energy $h\nu < 1 \text{ Ryd}$ will photoionize all elements whose first ionization potential is below that of hydrogen (e.g. C, Si) and harder photons may ionized a majority of the H I gas and place the heavy elements in higher ionization states.

Collisional processes, predominantly with electrons and hydrogen nuclei, may further ionize the medium for gas at $T > 10^4$ K.

Focusing on photoionization first, the population of galaxies and quasars at $z \sim 3$ is known to generate an extragalactic UV background (EUVB) which ionizes the majority of baryons in the universe (e.g. (41,42)). For gas with the relatively low H I column densities of our LLSs, one predicts that the EUVB has substantially ionized the hydrogen gas and any heavy elements that are present. To quantitatively assess this process and its impact on the metallicity estimates, we have calculated a series of photoionization models using the CLOUDY software package (43). We assumed that each LLS may be modeled as a series of layers with constant hydrogen density n_{H} , constant and low metallicity, and a plane-parallel geometry. We irradiated this gas with the Haardt and Madau EUVB model³ (quasars+galaxies) (14) evaluated at the redshift of each LLS (e.g. $J_{\nu} = 2.45 \times 10^{-22} \text{ erg s}^{-1} \text{ Hz}^{-1} \text{ cm}^{-2}$ at 1 Ryd for $z = 3.4$) and considered gas with a range of n_{H} values. It is standard practice to describe a given photoionization model by the ionization parameter $U \equiv \Phi/(n_{\text{H}}c)$ with Φ the flux of ionizing photons. Each model was restricted to have a total N_{HI} column density consistent with the observations.

In Fig. S5, we present the upper limits to the metallicity of the two LLSs as a function of n_{H} values. The figure indicates the limit imposed for the range of ions constrained by our observations. As a function of n_{H} , each curve shows the metallicity limit from a given ion according to the measured upper limit on its column density. The black symbols then trace the lowest metallicity imposed by the full set of measurements at each n_{H} value. In all cases we compare to the solar abundances of (44).

At high densities (low U values), the tightest limits are given by the lowest ionization stages of the heavy elements (Si^+ , O^0 , C^+). These set upper limits to the metallicity of $\lesssim 10^{-3} Z_{\odot}$. We emphasize, however, that such high densities are improbable. A gas with $n_{\text{H}} > 10^{-1} \text{ cm}^{-3}$ is predicted to have a neutral fraction $x_{\text{HI}} \equiv n_{\text{HI}}/n_{\text{H}} > 0.1$, but all of the LLSs that have been studied to date exhibit substantial absorption from higher ionization states of Si, C, and O. When analyzed as photoionized gas, one derives ionization parameters $\log U = -3$ to -1 (Fig. S6). At the respective redshift for the two LLSs, this implies a volume density $n_{\text{H}} < 10^{-2} \text{ cm}^{-3}$ which corresponds to an overdensity relative to the mean baryon density of $\rho/\rho_{\text{mean}} < 850$. As n_{H} decreases (and U increases), the heavy elements shift to higher ionization states and the limits on the gas metallicity become much more stringent. This is partly a result of tighter limits to the ionic column densities but it is primarily because our models are forced to match the observed N_{HI} value. At higher ionization parameter, the gas is more highly ionized and the total implied hydrogen column density is correspondingly larger ($N_{\text{H}} = N_{\text{HI}}/x_{\text{HI}}$). Therefore, at fixed metallicity this implies higher total column densities for the heavy elements. For the ionization parameters typically measured for LLSs ($U > 10^{-3}$), we set an upper limit to the gas metallicity (based on Si) of $Z < 10^{-4.2}(10^{-3.8})Z_{\odot}$ for LLS1134a (LLS0956B). This is a conservative value and also the most physically-motivated limit to the metallicity.

If the intensity of the ionization field is much higher than the assumed EUVB, the lack

³The results would be slightly different with a different shape for the radiation field, but the differences are much smaller than those related to varying the ionization parameter.

of substantial Si IV and C IV absorption imposes a tight limit to the metallicity, as evident from Fig. S5. Extreme scenarios in which most of the metals are in even higher ionization states are highly implausible since at $\log U \gg 1$ a neutral fraction $x_{\text{HI}} \ll -6$ would imply a total hydrogen column density $N_{\text{H}} \gg 10^{24} \text{ cm}^{-2}$. Further, if these two LLSs lie in proximity to a star forming galaxy, the ionization field is dominated by a softer spectrum. To explore this possibility, we have calculated a second set of CLOUDY models adding to the EUVB the contribution from a galaxy with star formation rate $100 M_{\odot} \text{ yr}^{-1}$. We have further assumed that the escape fraction of ionizing radiation is $f_{\text{esc}} = 0.1$ and that the LLSs are at 100 kpc from the star forming disks. Under these conditions, the ionization states of the metals do not differ substantially from our previous calculation. Indeed, at $N_{\text{HI}} = 10^{18} \text{ cm}^{-2}$, the inferred metallicity for LLS1134a is $Z < 10^{-4.0}$. Therefore, we conclude that the assumed limits of $\sim 10^{-4}$ for LLS1134a and LLS0956B are representative of the underlying gas metallicity in different plausible scenarios.

For gas with $T > 2 \times 10^4 \text{ K}$, collisional ionization is an important process for establishing the ionization state of the gas. If one assumes collisional ionization equilibrium, it is straightforward to set limits on the gas as a function of the gas temperature (45). For $T > 2.5 \times 10^4 \text{ K}$, the limits are yet lower than those suggested by the photoionization modeling. At $T \sim 5 \times 10^4 \text{ K}$, the lack of substantial Si III and C III constrains the metallicity at $Z < 10^{-6}(10^{-5})Z_{\odot}$ for LLS1134a (LLS0956B), while at higher temperatures, $T \sim 10^5 \text{ K}$, the upper limits on the Si IV and C IV column densities correspond to $Z < 3 \times 10^{-7}(10^{-6})Z_{\odot}$ for LLS1134a (LLS0956B). At temperatures below $T \sim 2.5 \times 10^4 \text{ K}$, we expect both collisional ionization and photoionization to contribute, with the latter dominating.

5 Comparison with Other Observations

To compare the limits on the metallicity for LLS1134a and LLS0956B with other observations, we search the literature for metallicity estimates of cosmic structures in the redshift interval $2 \lesssim z \lesssim 5$. The metal abundances in solar units as a function of the gas density are summarized in Fig. 1. Since we cannot guarantee completeness in our search, this figure offers only a qualitative assessment on the interval of metallicity reported in one or multiple studies which include large samples. Here we provide a description of the different data shown in the figure.

The range of densities and metals for the Ly α forest is taken from (8), who compile O VI absorption statistics at $z \sim 2.5$ using the line-fitting technique. These metallicities are consistent with other studies that are based on different analysis of the IGM (e.g. the pixel optical depth method (46)). Upper limits and statistical fluctuations around or below $Z \sim 10^{-3}$ have been also reported at densities $\rho/\rho_{\text{mean}} \sim 1$. These are represented in Fig. 1 using a downward arrow.

For the LLSs (here loosely defined in the interval $\log N_{\text{HI}} \sim 10^{16} - 10^{20.3} \text{ cm}^{-2}$), we search in the literature for published metallicity and densities between $z = 1.5 - 4.5$ (12, 13, 16, 25, 47–57). The range plotted in Fig. 1 brackets these observations. For this class of objects we also present the logarithmic mean and standard deviation based on our (nearly) complete com-

pilation. In addition to the metallicity, we gathered information on the ionization parameters, used to produce Fig. S6. ISM metallicity in damped Ly α systems has been measured with both quasars and γ -ray bursts (GRBs). In both cases, we adopt a number density $0.05 - 10 \text{ cm}^{-3}$ which is consistent with the densities for the ISM atomic phase (58, 59). For the quasar sample, we report the range of metallicity between $z = 2 - 5$ from (5), extended at the lower end with the metal poor sample of (60). For the GRB sample we adopt instead the metallicities presented in (61).

Spectroscopy of high redshift galaxies provide abundances from unresolved H II regions in star forming galaxies. Here, we adopt the metallicity in two samples of $z \sim 2$ and $z \sim 3$ galaxies from (6, 62). We adopt a range of densities typical of nearby H II regions (63). Several studies have revealed super-solar metallicity in the broad line regions of quasars. Here, we adopt a compilation of metallicity from a large sample of $z > 3.7$ quasars and we choose a density interval typically measured in the broad line region (63).

Finally, we present the metallicity in Milky Way halo stars. Stellar metallicity is often quoted using iron abundance, but the density of heavy elements is dominated by O, C, Ne, and other α -elements. We therefore consider the oxygen abundances presented in (64), extended at low metallicity with the star reported by (9). Although the inferred metallicity at the lower end suffers from considerable observational uncertainties (64), values at $Z \sim 10^{-3} Z_{\odot}$ are common in large compilations (65) even for stars with extremely low iron abundances. In fact, only a single star has been reported at $Z \sim 10^{-4} Z_{\odot}$ (9).

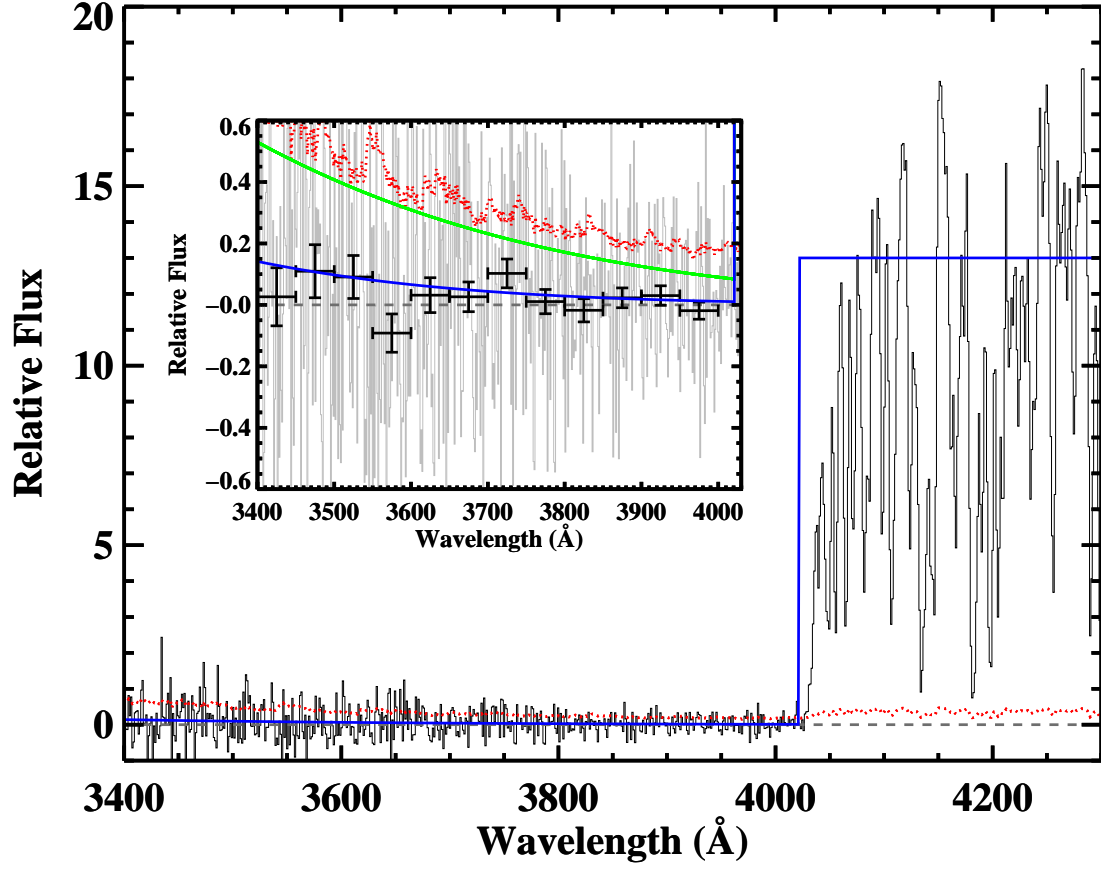


Figure S1: LRIS spectrum of J1134+5742 at the Lyman limit. Superimposed to the data, we show the flux decrement for a $N_{\text{HI}} = 10^{18.05} \text{ cm}^{-2}$ LLS (blue line) together with the error on the flux (red dotted line). In the inset, we show the data at full resolution (gray histogram) and in bins of 50 Å (crosses). A model of the Lyman limit opacity for $\log N_{\text{HI}} > 17.90$ (green line) is also shown.

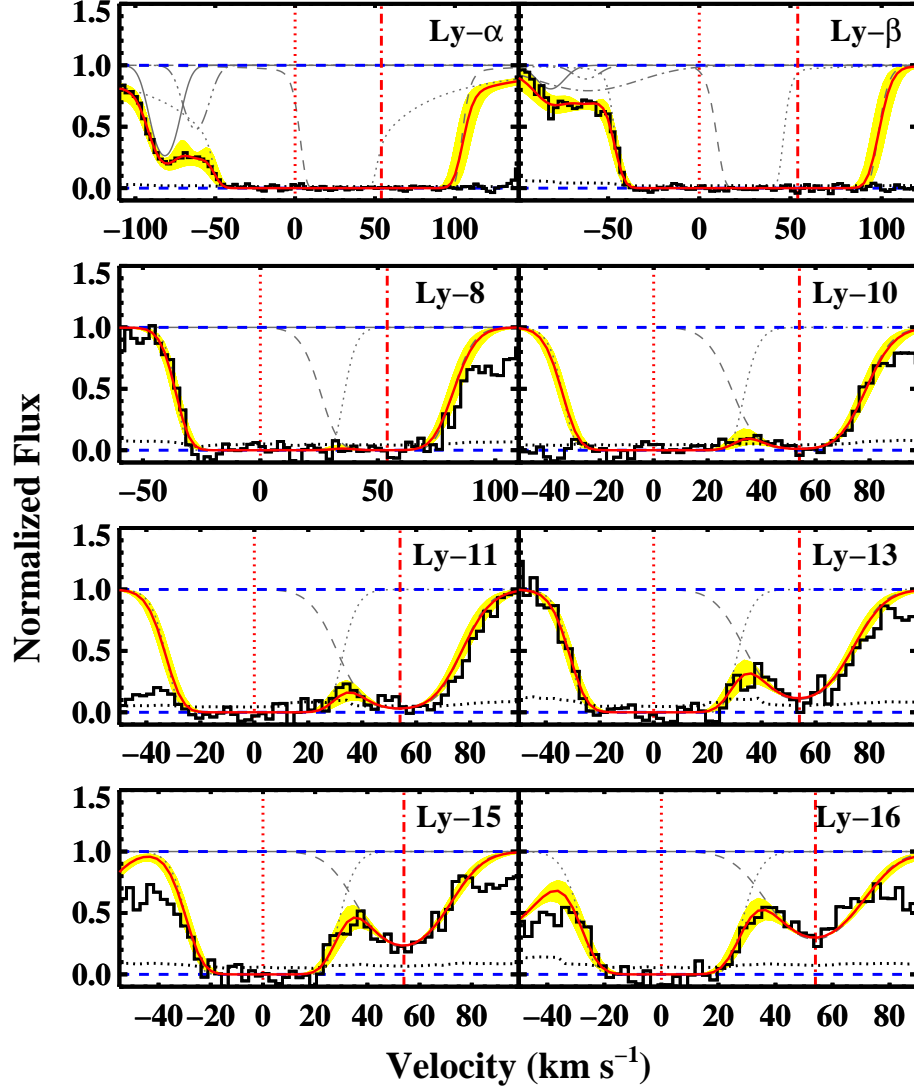


Figure S2: Gallery of the Lyman series transitions (black histograms) and best fit models (red lines) for LLS1134. The yellow shaded regions represent the 2σ errors on the line parameters. LLS1134a and LLS1134b are marked by vertical lines, while the dotted black lines indicate the 1σ error on the flux. Individual components included in the model are shown with gray lines.

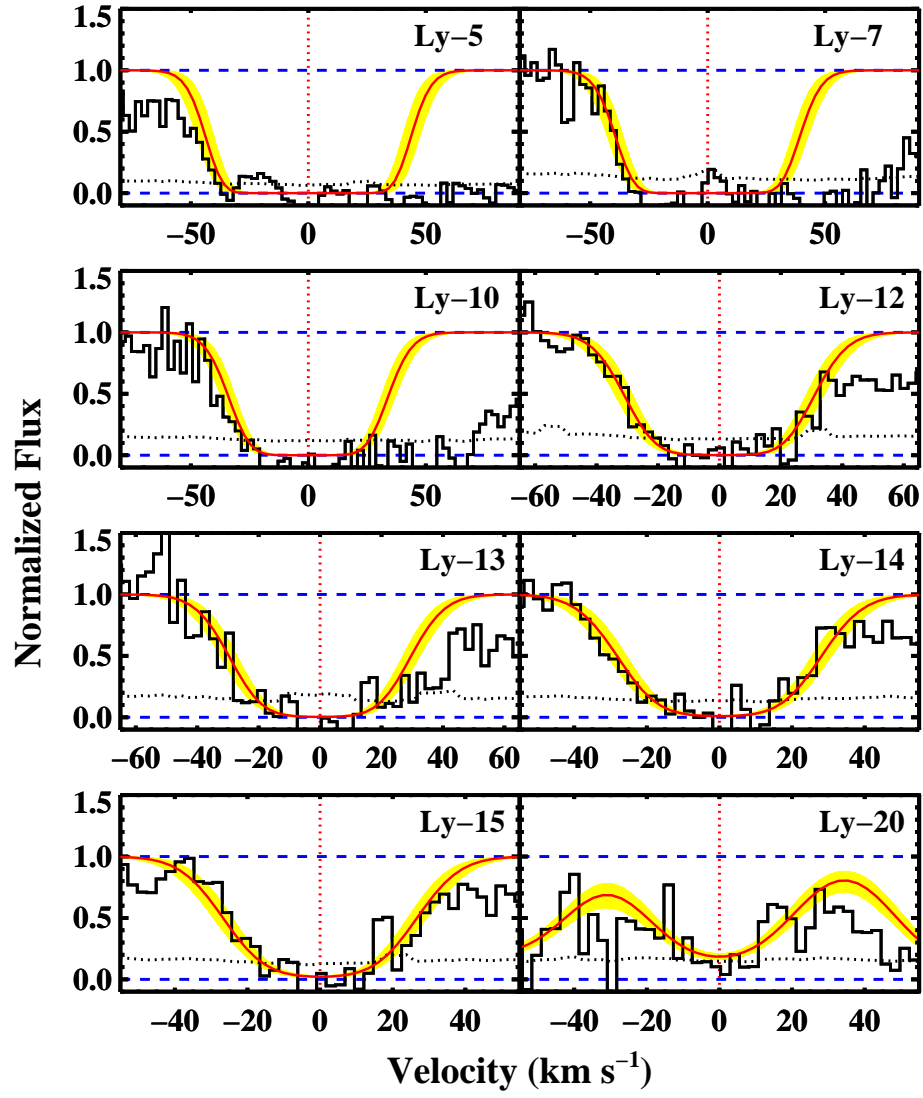


Figure S3: Same as Figure S2, but for LLS0956B.

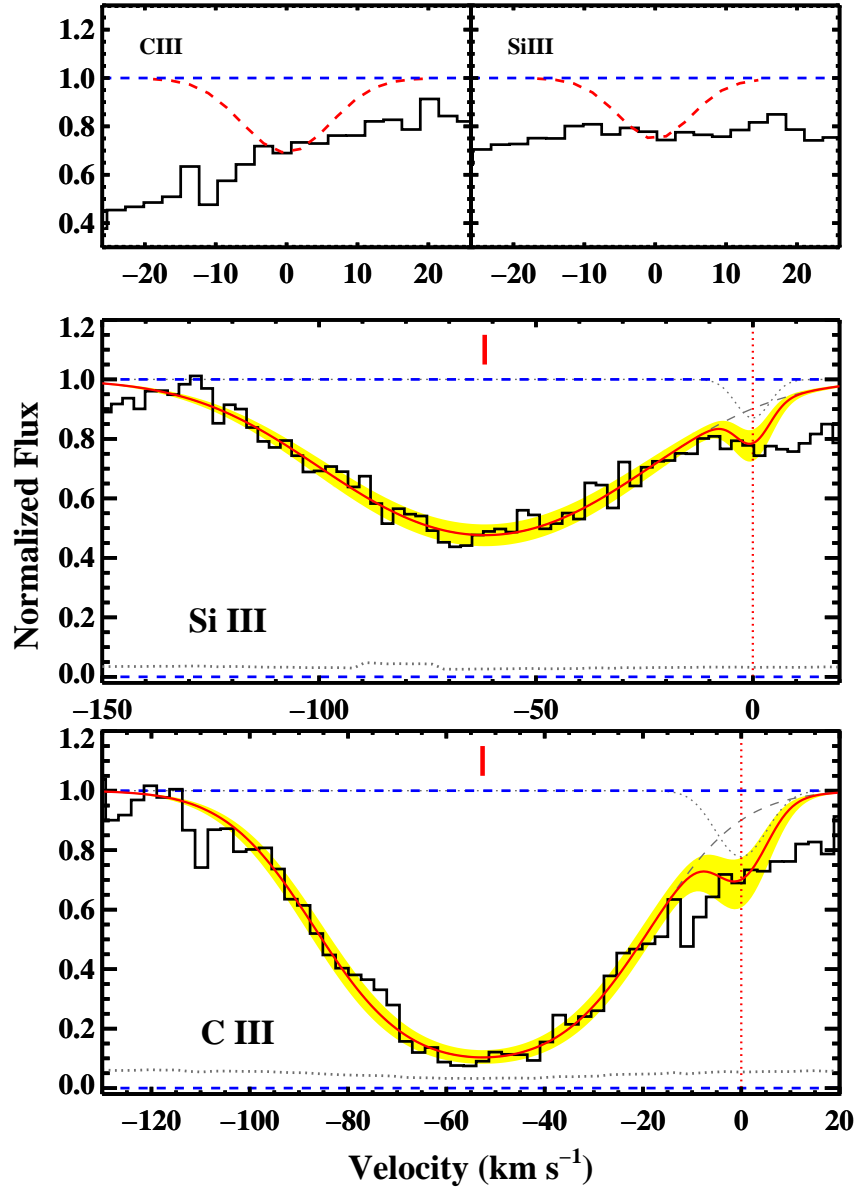


Figure S4: Top panels: C III 977 and Si III 1206 transitions for LLS1134a. Together with the HIRES data (black histograms), we display a model for the strongest lines that could be hidden by the IGM absorption (red dashed lines). In the bottom panels, we present a single component model (gray dashed line) for the IGM absorption that contributes to the opacity at the C III and Si III frequencies. Models for these transitions with the adopted column density limits are also shown (gray dotted line). In red, we display the combined two-component models, together with the corresponding 2σ errors on the line parameters. In all cases, we assume a Doppler parameter of 6.9 km s^{-1} for carbon and 5.3 km s^{-1} for silicon, as inferred from the hydrogen and deuterium lines.

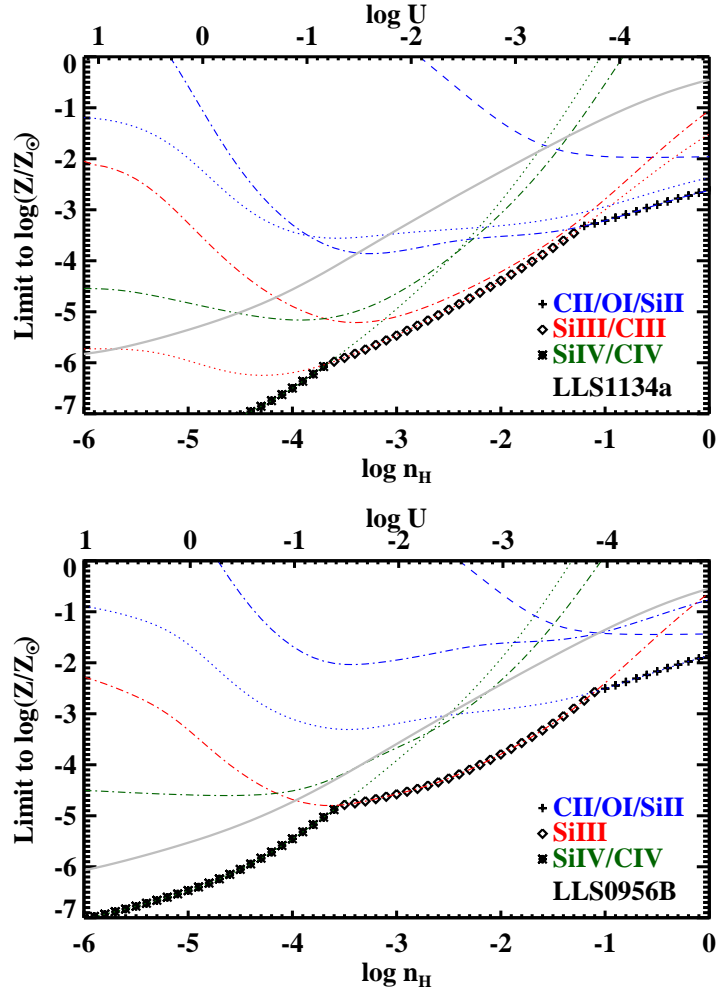


Figure S5: The two panels describe the metallicity limits to (top) LLS1134a and (bottom) LLS0956B as a function of the gas density n_{H} , assuming the Haardt and Madau EUVB radiation field (14). Each curve shows the metallicity limit for a given ion according to the upper limit on its column density. Elements C, O, and Si are traced by dotted, dashed, and dash-dot lines respectively. The black symbols then trace the lowest metallicity imposed by the full set of measurements at each n_{H} . The solid gray curves in the figure indicate the logarithm of the neutral fraction of the gas $x_{\text{HI}} \equiv n_{\text{HI}}/n_{\text{H}}$.

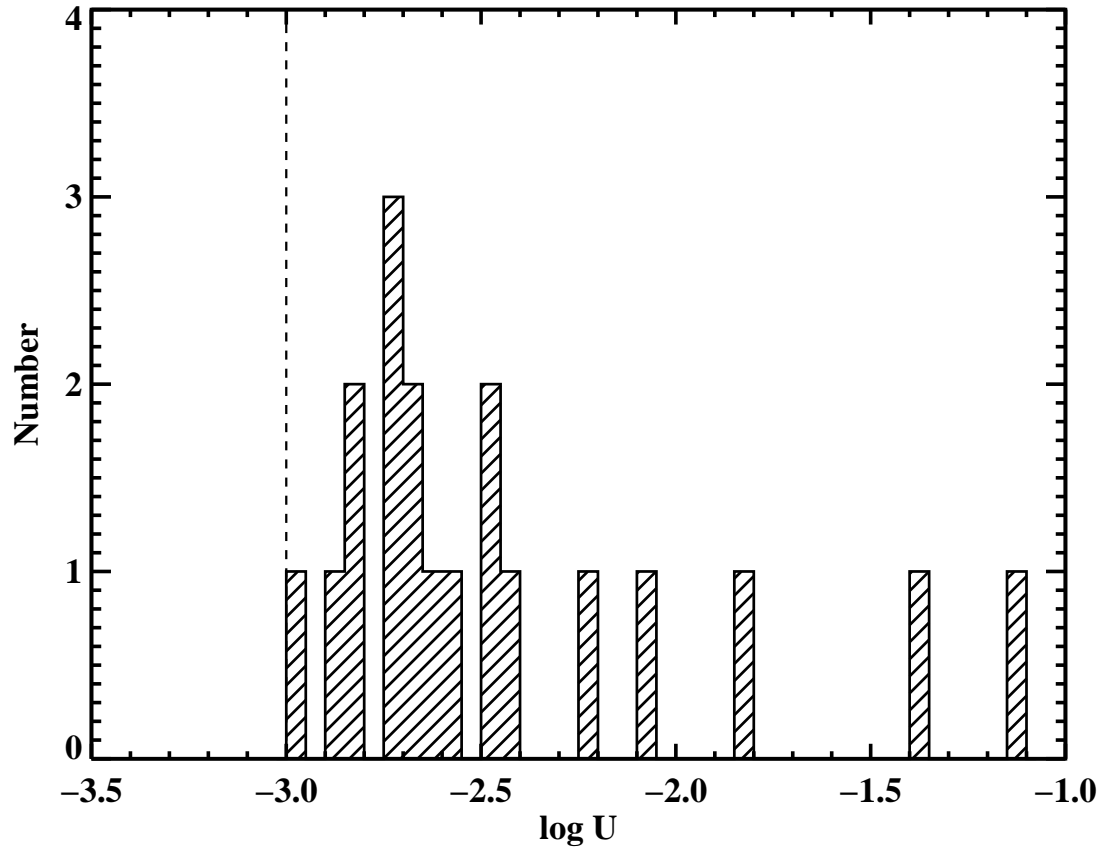


Figure S6: Distribution of the ionization parameter U for all the $z > 1.5$ LLSs reported to date in the literature. The value $U = 10^{-3}$ used in this analysis is marked with a dashed line.

Ion	z_{abs}	δv (km s ⁻¹)	Doppler parameter (km s ⁻¹)	Column density (log N)
D I	3.410883 ± 0.000004	0	10.2 ± 0.8	13.26 ± 0.04
H I	3.40997 ± 0.00002	-62	9.9 ± 1.9	12.99 ± 0.07
H I	2.7209 ± 0.0001	—	36.9 ± 9.2	13.05 ± 0.12
H I	3.410883 ± 0.000004	0	15.4 ± 0.3	17.94 ± 0.05
H I	3.41167 ± 0.00001	54	18.0 ± 0.9	16.71 ± 0.02

Table S1: Summary of the best-fit model for the LLS1134 hydrogen and deuterium absorption. For each ion we list: the redshift of the absorption, the velocity offset relative to the main hydrogen component, the Doppler parameter and the column density.

Ion	λ (Å)	$\log f$	LLS1134a		LLS0956B	
			$\log N$ (cm ⁻²)	W_0^a (mÅ)	$\log N$ (cm ⁻²)	W_0^a (mÅ)
C II	1334.5323	-0.8935	< 12.45	< 5.7	< 12.26	< 3.7
C III	977.0200	-0.1180	< 12.20	< 10.2	-	-
C IV	1548.1950	-0.7194	< 12.09	< 5.0	< 12.30	< 8.1
O I	1302.1685	-1.3110	< 12.76	< 4.2	< 12.50	< 2.3
Si II	1260.4221	0.0030	< 11.30	< 2.8	-	-
Si II	1526.7066	-0.8962	< 12.27	< 4.9	< 12.45	< 7.4
Si III	1206.5000	0.2201	< 11.40	< 5.4	< 11.21	< 3.5
Si IV	1393.7550	-0.2774	< 11.69	< 4.4	< 11.83	< 6.1
Fe II	1608.4511	-1.2366	< 12.59	< 5.2	< 12.72	< 7.0

^a The rest-frame equivalent width (W_0) is computed for the linear portion of the curve of growth.

Table S2: 2σ upper limits on the column density of metal ions and rest-frame equivalent widths. Rest frame wavelengths and oscillator strengths (f) from (66) are also listed.

Quasar	z_{abs}	$\log \text{D/H}$	$\log N_{\text{HI}}$	$[\text{X}/\text{H}]$
HS0105 + 1619	2.53600	-4.60 ± 0.04	19.42 ± 0.01	-2.00^a
Q0913 + 072	2.61843	-4.56 ± 0.04	20.34 ± 0.04	-2.37^a
Q1009 + 299	2.50357	-4.40 ± 0.07	17.39 ± 0.06	-2.5^b
J1134+5742	3.41088	-4.69 ± 0.13	17.95 ± 0.05	$< -4.2^{b,c}$
Q1243 + 3047	2.52566	-4.62 ± 0.05	19.73 ± 0.04	-2.79^a
SDSSJ1558 – 0031	2.70262	-4.48 ± 0.06	20.67 ± 0.05	-1.47^a
Q1937 – 1009	3.57220	-4.48 ± 0.04	17.86 ± 0.02	$-2.7, -1.9^{b,d}$
Q2206 – 199	2.07624	-4.78 ± 0.09	20.43 ± 0.04	-2.04^a

^a Metallicity obtained using oxygen. ^b Metallicity obtained using silicon. ^c This work. ^d The authors report metallicities for two components. Data from (2, 3, 16, 49–51, 67, 68).

Table S3: Deuterium abundances in $z > 2$ absorption line systems.